Droplets walking in a rotating frame: from quantized orbits to multimodal statistics

Daniel M. Harris and John W. M. Bush†

Department of Mathematics, Massachusetts Institute of Technology, Cambridge, MA 02139, USA

We present the results of an experimental investigation of a droplet walking on the surface of a vibrating rotating fluid bath. Particular attention is given to demonstrating that the stable quantized orbits reported by Fort *et al.* (*Proc. Natl Acad. Sci.*, vol. 107, 2010, pp. 17515–17520) arise only for a finite range of vibrational forcing, above which complex trajectories with multimodal statistics arise. We first present a detailed characterization of the emergence of orbital quantization, and then examine the system behaviour at higher driving amplitudes. As the vibrational forcing is increased progressively, stable circular orbits are succeeded by wobbling orbits with, in turn, stationary and drifting orbital centres. Subsequently, there is a transition to wobble-and-leap dynamics, in which wobbling of increasing amplitude about a stationary centre is punctuated by the orbital centre leaping approximately half a Faraday wavelength. Finally, in the limit of high vibrational forcing, irregular trajectories emerge, characterized by a multimodal probability distribution that reflects the persistent dynamic influence of the unstable orbital states.

Key words: drops, Faraday waves, waves/free-surface flows

---

1. Introduction

Louis de Broglie (1926, 1987) proposed a pilot-wave theory for microscopic quantum particles known as the 'double-wave solution', according to which particles are guided by an extended monochromatic wave field, and the resulting particle motion is consistent with the statistical predictions of standard quantum theory. Recently, Y. Couder and co-workers discovered the first macroscopic pilot-wave system, a hydrodynamic system in which an oil droplet propels itself laterally on the surface of a vibrating fluid bath by virtue of a resonant interaction with its own wave field (Protière, Boudaoud & Couder 2006; Eddi *et al.* 2011). Despite the complexity of the underlying pilot-wave dynamics, it has been demonstrated in two hydrodynamic quantum analogue experiments that a coherent multimodal statistical behaviour may emerge, in single-particle diffraction (Couder & Fort 2006) and for walkers in confined geometries (Harris *et al.* 2013). The current study explores a third hydrodynamic quantum analogue system that exhibits multimodal statistics and is the first to systematically characterize their emergence.

Coalescence of a droplet placed on the surface of a fluid bath can be prevented by vertical vibration of the bath (Walker 1978; Couder *et al.* 2005). The air layer
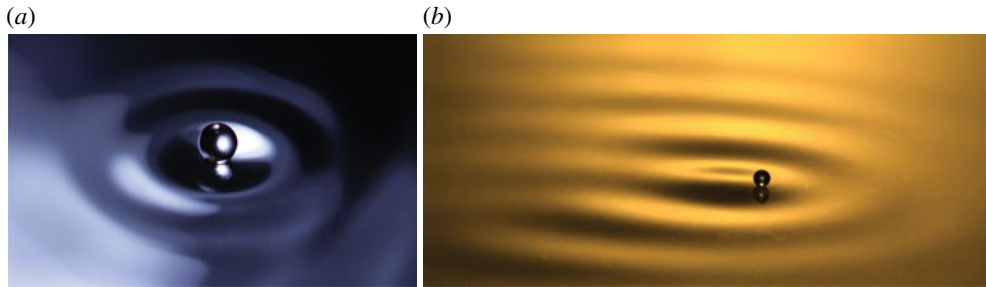
† Email address for correspondence: bush@math.mit.edu

FIGURE 1. (Colour online) (*a*) An oil droplet bouncing on the surface of a vibrating fluid bath. (*b*) A droplet walking laterally across the surface of the bath, self-propelled by a resonant interaction with its own Faraday wave field. The drop diameter is approximately 0.9 mm in both images. Photographs by D. M. Harris.

separating the droplet and the bath is sustained provided the drop's contact time is less than the time required for the intervening air layer to drain to a critical thickness at which van der Waals forces initiate coalescence. There is a critical value of the forcing acceleration, below which the drop coalesces with the bath, and above which it bounces with the forcing frequency f. As the driving acceleration is increased progressively, millimetric droplets exhibit a rich dynamics that may include a period doubling cascade, temporal chaos and other quasi-periodic bouncing states (Protière *et al.* 2006; Eddi *et al.* 2008; Moláček & Bush 2013*a*; Wind-Willassen *et al.* 2013).

In the absence of a droplet, provided a critical acceleration amplitude is exceeded, $\gamma > \gamma_F$, the surface of a fluid bath subjected to a vertical acceleration $\gamma \sin(2\pi f t)$ becomes unstable to a field of Faraday waves with frequency $f/2$ (Faraday 1831; Benjamin & Ursell 1954). Below this Faraday threshold, $\gamma < \gamma_F$, a localized field of waves can still be excited by a bouncing droplet. When the drop's bouncing frequency is commensurate with that of its Faraday wave field, $f/2$, resonance is achieved between the droplet and the bath. If the waves are of sufficient amplitude, the bouncing state can be superseded by a walking state (figure 1) in which the droplet moves laterally along the surface of the bath, nudged along at each bounce by its own wave field (Protière *et al.* 2006; Eddi *et al.* 2011; Moláček & Bush 2013*b*). In the absence of boundaries or external forces, the walking droplet, henceforth 'walker', may move along the surface of the bath in a straight line at a uniform speed. In addition to the simple resonant walking states in which the droplet's vertical motion and its wave both have frequency $f/2$, several exotic walking states with relatively complex vertical dynamics have now been predicted and observed (Moláček & Bush 2013*b*; Wind-Willassen *et al.* 2013).

The walker's lateral velocity is influenced by the local slope of the interface at impact, this slope being determined by the sum of the waves generated by its previous impacts. Specifying the properties of the droplet at a given instant is thus insufficient to predict its evolution: one must also have a complete description of the underlying wave field, which depends explicitly on the walker's history. Eddi *et al.* (2011) thus characterized the dynamics in terms of the walker's 'path memory'. For long path memory or equivalently 'high memory' (i.e. near the Faraday threshold), the walker's trajectory is more strongly influenced by its history (Eddi *et al.* 2011; Moláček & Bush 2013*b*). To study the walker's dynamics theoretically, Moláček & Bush (2013*b*) developed a trajectory equation, which was recast into integro-differential form by

Oza, Rosales & Bush (2013*b*). The resulting theory rationalizes both the observed dependence of walking speed on memory, and the stability of the walking states.

Several experiments have demonstrated that in the long path-memory regime, the behaviour of walking droplets is reminiscent of that of quantum particles (Bush 2010). Couder & Fort (2006) investigated individual walkers impinging on both single- and double-slit geometries. In both cases, they observed a distinct wavelike statistical pattern in the walker's deflection angle, a pattern that emerges after many repetitions of the same experiment with similar initial conditions. The wavelike statistical pattern was shown to correspond closely to the far-field amplitude of a plane wave with the Faraday wavelength passing through the slit geometry. Harris *et al.* (2013) examined a single walker confined to a circular geometry or 'corral' and demonstrated that, while the resulting trajectory is highly disordered, a coherent wavelike statistical pattern emerges to describe the walker's position. This statistical pattern is well described by the amplitude of the most unstable Faraday wave mode of the corral. The corral system is thus reminiscent of the quantum corral experiments (Crommie, Lutz & Eigler 1993), provided the Faraday wavelength is identified with the de Broglie wavelength of the trapped electrons. In each of the experiments, the wavelike probability distribution assumes a multimodal form, with the spacing of the peaks defined by the wavelength of the guiding wave field. Here, we will discuss a third experimental configuration in which multimodal statistics emerge from walker dynamics in the high-memory limit.

The motion of droplets walking on a rotating bath was first considered by Fort *et al.* (2010), who observed that walkers follow circular orbits in the rotating frame of reference. One expects an object moving with constant speed u_0 in a rotating frame to follow circular orbits with a radius that varies continuously with the imposed rotation rate. Specifically, balancing the radially inwards Coriolis force $F_\Omega = 2m\Omega u_0$ and the inertial force $F_c = mu_0^2/r_0$ indicates an inertial orbit with radius $r_0 = u_0/2\Omega$ and frequency $\omega = u_0/r_0 = -2\Omega$. In what follows, we shall refer to an inertial orbit as a circular orbit in which the Coriolis and inertial forces balance. Fort *et al.* (2010) demonstrated that, at low memory, the orbital radius of the walker indeed varies continuously with the rotation rate. However, at high memory, only discrete bands of possible orbital radii exist, the spacing between them being roughly equal to half the Faraday wavelength. They demonstrated that the observed orbital quantization results from the droplet's interaction with its own wave field. While they documented the transition from continuous to discrete orbits, they did not examine the system behaviour in the high-memory limit, where, as we shall see here, the orbits become unstable. Moreover, they did not report the precise amplitudes of the vibrational forcing used, making quantitative comparison to the present study or our group's associated theoretical developments (Oza *et al.* 2013*a*) difficult. As we shall see in what follows, the system behaviour is extremely sensitive to the forcing amplitude in the long memory limit.

Owing to the analogous form of the Coriolis force acting on a mass in a rotating frame and the Lorentz force acting on a charge in the presence of a uniform magnetic field, Fort *et al.* (2010) were able to draw an analogy between their quantized orbits and Landau levels, with the Faraday wavelength playing the role of the de Broglie wavelength. Eddi *et al.* (2012) demonstrated that the distance between a pair of orbiting walkers is likewise quantized, but can be modulated by rotating the bath. Specifically, the orbital radius increases or decreases continuously with the rotation rate, according to whether the orbiting pair is co- or counter-rotating relative to the bath. The same Coriolis–Lorentz analogy suggests that this orbital level splitting is
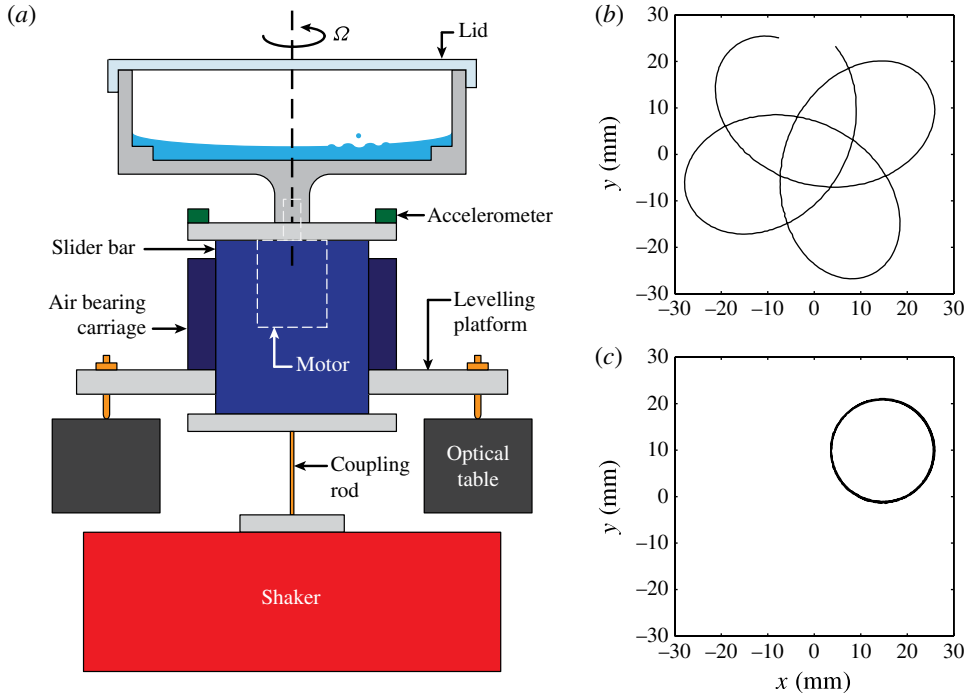
FIGURE 2. (Colour online) (*a*) Schematic of the experimental set-up. An electromagnetic shaker drives a rotating fluid tray, interfaced by a thin coupling rod and linear air bearing. The shaker is mounted onto a massive levelling platform (not shown). (*b*) Sample trajectory of a walker in the laboratory frame of reference with $\gamma/\gamma_F = 0.822 \pm 0.006$, $u_0 = 9.0$ mm s^{-1} and $\Omega = 0.61$ rad s^{-1}. (*c*) Same trajectory in the rotating frame of reference. The origin ($x = 0$, $y = 0$) in panels (*b*) and (*c*) represents the bath's centre of rotation.

analogous to the Zeeman effect whereby spectral lines are split in the presence of a magnetic field (Eddi *et al.* 2012).

The present work builds upon the work of Fort *et al.* (2010), but focuses on the system behaviour in the high-memory limit. In §2, the experimental methods are described. In §3, we present a detailed experimental exposition of the emergence of quantized orbital radii, the number of which are shown to increase with system memory. Subsequently, in §4, focus is given to characterizing the behaviour of walkers at higher memory than previously considered, where quantized orbits give way to wobbling states of increasing complexity. Finally, in §5, it is shown that, at even higher memories, the walker may escape its confinement to a single orbital level and carry out complex motion marked by multimodal statistics. Our results are summarized in §6.

2. Experimental methods

A schematic of the experimental set-up is shown in figure 2(*a*). For the present experiments, we use a circular tray of inner diameter 146 mm and depth 38 mm filled to a depth of $H = 7.0$ mm with a silicone oil of density $\rho = 950$ kg m^3, surface tension $\sigma = 0.0206$ N m^{-1} and kinematic viscosity $\nu = 20.9 \pm 0.1$ cS. The viscosity is highly sensitive to temperature and is estimated using fluid temperature measurements,

made with an infrared thermometer, and an empirical relationship between temperature and viscosity provided by the oil manufacturer (Clearco). A shallow border of depth 1.0 mm and width 9.5 mm surrounds the deeper central part of the fluid bath, which avoids complications that would otherwise arise from the meniscus at the tray's outer wall, a technique that has been employed in previous investigations of walking droplets (Eddi *et al.* 2009; Harris *et al.* 2013). The fluid tray is vibrated sinusoidally at frequency $f = 80$ Hz with an acceleration amplitude γ. Above a critical acceleration amplitude γ_F, standing Faraday waves spontaneously form with frequency $f/2$ and wavenumber k_F that can be estimated using the standard water-wave dispersion relation (Kumar 1996)

$$(\pi f)^2 = \left(g k_F + \frac{\sigma k_F^3}{\rho} \right) \tanh k_F H, \qquad (2.1)$$

where g is the gravitational acceleration. For our parameters, this approximation yields a Faraday wavelength $\lambda_F = 2\pi/k_F = 4.75$ mm, consistent with that observed. The Faraday threshold γ_F is measured to be $4.08 \pm 0.07g$ with the variation resulting from the high sensitivity of the Faraday threshold to temperature (here approximately $0.08g\ {}^\circ\text{C}^{-1}$), as arises through the temperature dependence of surface tension and viscosity. The Faraday threshold and temperature were measured and recorded at the beginning and end of each experiment. All experiments reported in this work are conducted below the Faraday threshold; thus, in the absence of a droplet, the bath would remain flat.

The present experiments require high resolution and careful control of the vibrational forcing. We use an air-cooled electromagnetic shaker (Data Physics, V55) with an external power amplifier (Data Physics, PA300E) to drive the fluid bath. Regrettably, most shakers feature flexure-type suspensions that are plagued with undesirable resonances that often lead to non-uniform and multi-directional vibration. In order to avoid such effects, we employ a system similar to that developed by Goldman (2002) for studies of vibrated granular materials (de Bruyn *et al.* 2001; Reis, Ingale & Shattuck 2007). The system includes a linear air bearing with square cross-section (Nelson Air Corp., 10.2 cm × 10.2 cm cross-section) interfacing the payload and the driver, effectively restricting the motion to a single vertical axis while also minimizing any undesirable angular motion. The air bearing carriage is mounted onto a heavy aluminium platform, which can be levelled using three micrometer screws resting on an optical table with a centred through-hole. The slider bar (which slides through the fixed air bearing carriage) is connected to the shaker via a thin coupling rod that is designed to avoid buckling, but to be relatively compliant laterally. The lateral stiffness of the air bearing is several orders of magnitude greater than that of the coupling rod, so that any non-axial motion generated by the shaker is taken up in deflection of the coupling rod and thereby not transmitted to the payload. We use two miniature piezoelectric accelerometers (PCB, 352C65) mounted in diametrically opposed locations atop the slider bar to measure the vibration amplitude, which is specified and monitored using a data acquisition system (NI, USB-6343) and custom Labview software. Closed loop feedback control maintains the vibration amplitude to within $\pm 0.005g$.

In addition to continuously vibrating the fluid tray, we rotate the tray about a vertical axis with angular rate Ω using a stepper motor (Mercury Motors, SM-42BYG011) mounted in the vibrating frame, whose speed and sense are specifiable via software. The rotation rate Ω is varied from 0 to 5.5 rad s^{-1} in the current experiments. At the maximum rotation rate considered, the fluid surface assumes a

parabolic shape with minimum depth at the centre of the tray of 2.9 mm. Nevertheless, the Faraday and walking thresholds remain nearly unchanged, provided the depth exceeds 2.5 mm (Eddi *et al.* 2009). We also note that the radially outward centrifugal force resulting from the system rotation is precisely balanced by the inward interfacial force imparted during impact on the parabolic bath surface, so that a stationary bouncing droplet will remain stationary in the rotating frame (Fort *et al.* 2010; Oza *et al.* 2013*a*). Our two principal control parameters are thus the relative forcing acceleration amplitude γ/γ_F and the rotation rate of the bath Ω. The acceleration amplitude of the forcing γ is related to the memory parameter, which can be defined as

$$M_e(\gamma/\gamma_F) = \frac{T_d}{T_F(1 - \gamma/\gamma_F)}, \qquad (2.2)$$

where T_d is the decay time of the waves in the absence of vibration and $T_F = 2/f$ is the period of the Faraday waves (Eddi *et al.* 2011; Moláček & Bush 2013*b*). The memory parameter M_e gives an indication of the number of previous bounces that contribute to the instantaneous guiding wave field. Note that γ/γ_F and M_e are monotonically related for the parameter regime of interest ($\gamma/\gamma_F < 1$), and that, as γ/γ_F approaches 1, M_e approaches ∞. Thus 'high memory' is synonymous with 'high forcing amplitude', and the two are used interchangeably henceforth.

We create droplets of radius $R_d = 0.40\text{--}0.43$ mm by rapidly extracting a submerged needle from the fluid bath (Protière *et al.* 2006). A transparent lid is placed on the tray to avoid the effects of ambient air currents. We then measure the walking speed u_0 of the droplet in the absence of rotation, which is found to be between 9.5 and 12.6 mm s^{-1}. The vertical motion of the walkers used in this study is completely period-doubled and corresponds to the $(2, 1)^2$ walking mode (Moláček & Bush 2013*b*; Wind-Willassen *et al.* 2013). Rotation is then applied and, before data are collected, we wait at least one minute, which significantly exceeds both the spin-up time of the fluid ($h_0^2/\nu \sim 2.5$ s) and the characteristic decay time of the walker's wave field ($T_F M_e < 4$ s). The walker's motion is filmed from above at 20 frames per second by a charge-coupled device (CCD) camera (AVT, Manta G-125) that has been levelled and aligned with the rotation axis of the tray. The trajectory of the walker in the laboratory frame is then determined using particle tracking software. In order to minimize spurious boundary effects, if the walker passed within $5.5\lambda_F$ (26.1 mm) of the submerged barrier, the data were discarded. Within this distance, the trajectory was noticeably influenced by the boundary at high memory; otherwise, the walker's motion and statistical behaviour were independent of its proximity to the boundary. A marker on the outer edge of the tray is also tracked, allowing for determination of the angle of the tray in each image, and for the transformation of the trajectory into the rotating frame. An example of a walker trajectory in the laboratory frame is given in figure 2(*b*), with the corresponding trajectory in the rotating frame in figure 2(*c*). Orbital radii and the local radius of curvature are calculated using the method described in the Appendix, with $\alpha = \pi/4$ for data presented in figures 4–9 and $\alpha = \pi/2$ for figures 10–12. Unless otherwise noted, error bars represent plus and minus one standard deviation of the measured quantity of interest.

3. The emergence of quantization

How does memory, specifically the proximity to the Faraday threshold, influence the dynamics of a walker in a rotating frame? Sample wave fields corresponding to an
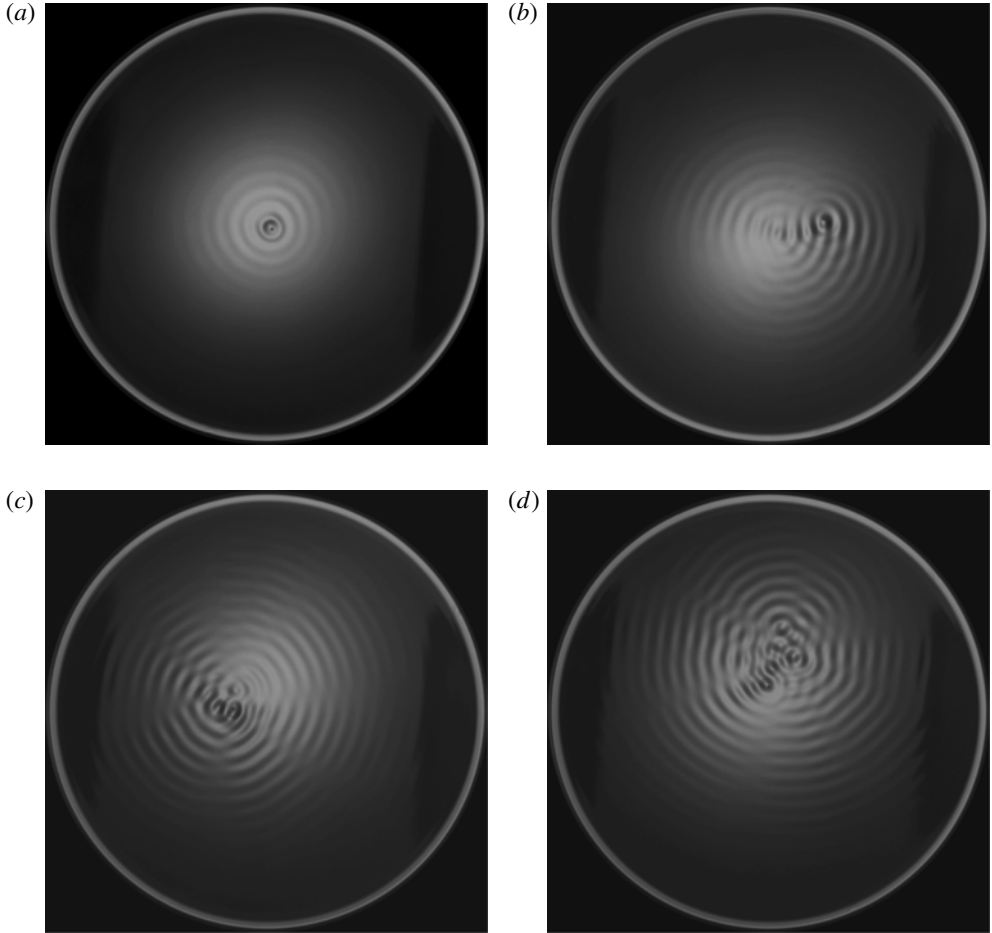
FIGURE 3. Wave fields generated by a walking droplet of radius $R_d = 0.4$ mm in a rotating frame ($\Omega = 0.79$ rad s^{-1}) as the driving acceleration is increased: (*a*) $\gamma/\gamma_F = 0.862 \pm 0.006$; (*b*) $\gamma/\gamma_F = 0.968 \pm 0.006$; (*c*) $\gamma/\gamma_F = 0.984 \pm 0.006$; (*d*) same conditions as (*c*), image taken 10.1 s later.

identical walker with increasing memory are shown in figure 3(*a–d*). At low memory (figure 3*a*) the wave field is nearly centred on the droplet, prescribed primarily by its most recent impact. As the memory is increased (figure 3*b*), the wave field is more persistent; consequently, in executing a circular orbit, the droplet interacts with its own wake. There is thus an influence of the walker's previous orbit on its present dynamics. At very high memory, as in figure 3(*c,d*), the wave field is considerably more complex, the form of which both reflects and perpetuates an irregular trajectory. The images in figure 3(*c,d*) are taken from a single experiment at very high memory, where the wave field is continuously evolving. In figure 3(*a–c*), note that the lateral extent of the wave field increases with memory. We proceed by considering walkers following regular circular trajectories.

In figure 4 we report the observed dependence of the orbital radii r_0 on the rotation rate Ω at four different values of memory. At low memory, we find that all orbital radii are accessible, and that the orbital radius r_0 decreases continuously and
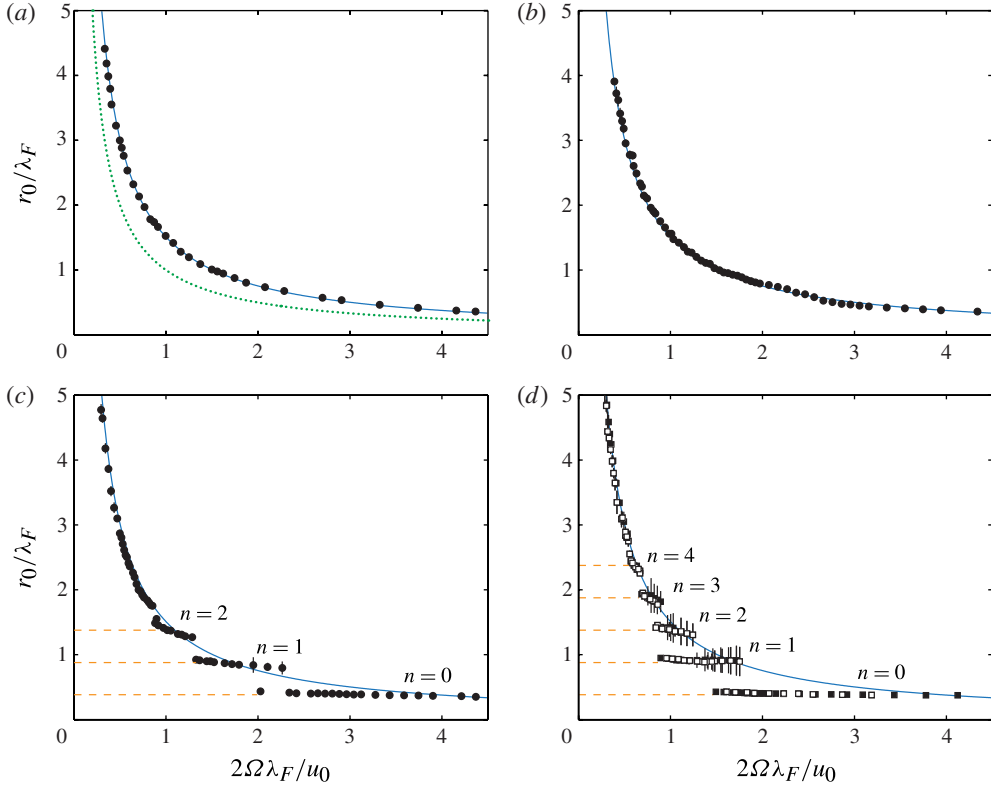
FIGURE 4. (Colour online) The observed dependence of the orbital radius r_0 on the rotation rate of the bath Ω: (a) $\gamma/\gamma_F = 0.822 \pm 0.006$ with $u_0 = 9.0$ mm s^{-1}; (b) $\gamma/\gamma_F = 0.922 \pm 0.004$ with $u_0 = 9.5$ mm s^{-1}; (c) $\gamma/\gamma_F = 0.954 \pm 0.006$ with $u_0 = 12.0$ mm s^{-1}; (d) $\gamma/\gamma_F = 0.971 \pm 0.004$ with $u_0 = 10.9$ mm s^{-1} (■) and 11.7 mm s^{-1} (□). The dotted line in panel (a) represents the standard prediction for inertial orbits, $r_0 = u_0/2\Omega$, while the solid line represents the modified relationship, $r_0 = au_0/2\Omega$, with a best-fitted value $a = 1.51$. The solid line is identical in all four panels, and is shown for the sake of comparison with the low-memory result. The horizontal dashed lines in panels (c) and (d) are the zeros of $J_0(k_F r)$, which correspond closely to the radii of the observed quantized orbital levels (Oza *et al.* 2013*a*).

monotonically with increasing rotation rate Ω (figure 4*a*). As was reported by Fort *et al.* (2010), there is an offset from the standard prediction for inertial orbits so that

$$r_0 = a\frac{u_0}{2\Omega}. \tag{3.1}$$

The data in figure 4(*a*) is best-fitted with an offset value of $a = 1.51$, shown in the plot as a solid line, indicating that the orbits are larger than expected. This is consistent with the results of Fort *et al.* (2010), who reported $1.2 \leqslant a \leqslant 1.5$ for all oil and forcing frequency combinations considered. This offset results from an outward radial wave force due to the influence of the waves generated by the most recent impacts. The dependence of the magnitude of this offset on the system parameters is rationalized in our theoretical treatment of the problem (Oza *et al.* 2013*a*). As the driving is increased further (figure 4*b*), a subtle deviation from the low-memory result begins to emerge at small radius (near $r_0/\lambda_F \approx 0.6$), although the curve remains continuous and

all radii accessible. More dramatic changes are apparent at the next value of memory considered (figure 4c), where the curve is no longer continuous, and several bands of radii become inaccessible. This leads to the emergence of three discrete orbital levels, $n = 0$, 1 and 2. Moreover, there is an orbital degeneracy: multiple radii are possible for a given rotation rate. Increasing the memory further (figure 4d) results in the emergence of additional quantized levels and heightened orbital degeneracy. The quantized radii are centred on the zeros of $J_0(k_F r)$ (represented by the dashed horizontal lines), which are nearly half multiples of the Faraday wavelength, a result rationalized in our theoretical treatment of the problem (Oza *et al.* 2013a).

   From the results in figure 4, a clear picture of the origins of orbital quantization has now emerged. As the memory is increased, the first variance from the low-memory result arises at the smallest radii, with the deviations propagating progressively upwards along the curve as the memory is increased. This progression is consistent with an intuitive understanding of the role of path memory. The smallest orbits have the smallest orbital period; thus, the walker's wake will have decayed the least after a single orbit. Consequently, walkers in the tightest orbits, as arise at higher rotation rates, will be most strongly affected by their past. The observed quantization is thus a direct result of memory. It also follows that, for sufficiently large orbits at any memory, the data should revert to the low-memory curve. This is precisely what is observed in our experiments; the data fall along the low-memory curve beyond the highest quantized level observed (figure 4c–d). For large orbits, the orbital period is much greater than the characteristic decay time of the Faraday waves; thus, the walker's prior orbits do not influence its dynamics.

   Another quantity readily measured is the walker's orbital frequency $\omega = u/r_0$. For standard inertial orbits, we recall $\omega = -2\Omega$. Assuming that the walker maintains a speed close to its free speed ($u \approx u_0$), we can rearrange the low-memory result (3.1) to find

$$\omega = -\frac{2\Omega}{a}. \tag{3.2}$$

We note that the walking speed in orbit u differs slightly from its free speed u_0 by no more than 6 % at the lowest memory considered ($\gamma/\gamma_F = 0.822$) and by no more than 12 % at the highest memory considered here ($\gamma/\gamma_F = 0.971$). Consequently, (3.2) should still provide a reasonable description of the orbital frequencies at low memory. In our experiments, we measure the speed and orbital radius, from which we calculate the orbital frequency $\omega = u/r_0$. The dependence of the orbital frequency on rotation rate is presented in figure 5, each panel of which corresponds to its counterpart in figure 4. At low memory (figure 5a), the data follow a line well described by (3.2) using $a = 1.51$ as determined previously. The orbital frequencies are thus less than those expected for standard inertial orbits. At higher memory (figure 5b), the deviation from the low-memory result becomes apparent at high rotation rates (i.e. for small radii). A significant difference is apparent in figures 5(c) and 5(d), where the curves are no longer continuous, but discrete bands of possible orbital frequencies emerge. The quantization in orbital frequency is a consequence of that in orbital radius. We note that, in all cases, for sufficiently low frequencies (large orbital radii), the data closely follow the linear relationship expected at low memory.

   From what we have seen thus far, one might anticipate the emergence of further quantized levels at higher memory. We shall proceed by demonstrating that, conversely, the circular orbits become unstable at high memory. The increased size of the error bars at levels $n = 1, 2$ and 3 in figure 4(d) does not reflect an increased experimental
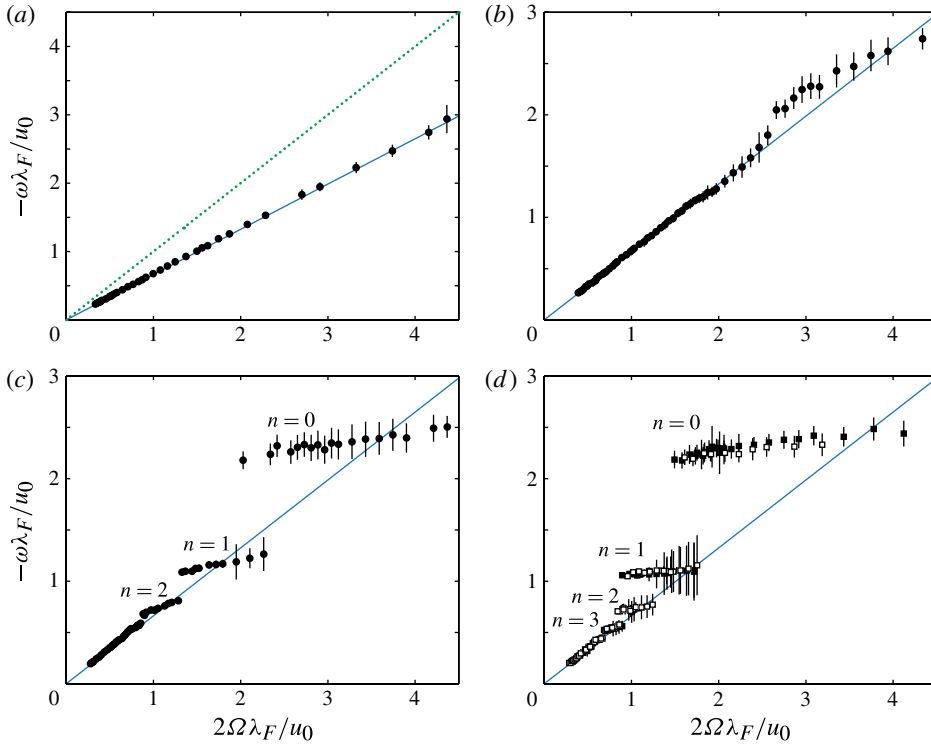
FIGURE 5. (Colour online) The observed dependence of the orbital frequency ω on the rotation rate of the bath Ω: (*a*) $\gamma/\gamma_F = 0.822 \pm 0.006$ with $u_0 = 9.0$ mm s^{-1}; (*b*) $\gamma/\gamma_F = 0.922 \pm 0.004$ with $u_0 = 9.5$ mm s^{-1}; (*c*) $\gamma/\gamma_F = 0.954 \pm 0.006$ with $u_0 = 12.0$ mm s^{-1}; (*d*) $\gamma/\gamma_F = 0.971 \pm 0.004$ with $u_0 = 10.9$ mm s^{-1} (■) and 11.7 mm s^{-1} (□). The dotted line in panel (*a*) represents the standard prediction for inertial orbits, $\omega = -2\Omega$, while the solid line (plotted in each panel) represents the modified relationship suggested by (3.2), $\omega = -2\Omega/a$, with $a = 1.51$.

error, but rather oscillations in the orbital radius, as arise for 'wobbling' orbits. This effect was not reported by Fort *et al.* (2010), presumably due to the lower forcing amplitudes considered in their study.

4. Wobbling orbits

We now turn our attention to wobbling orbits, as are characterized by an oscillation in both the radius and the radius of curvature R along the trajectory. We note that the possibility of wobbling orbits was originally suggested by the linear stability analysis in our theoretical treatment of the problem (Oza *et al.* 2013*a*). We will focus on wobbling orbits at the $n = 1$ orbital level, as a preliminary exploration suggested that they occur over the largest range of control parameters. We adopt the following procedure. At a fixed forcing amplitude ($\gamma/\gamma_F > 0.96$) we first increase the rotation rate gradually from zero until the walker enters the $n = 1$ orbital level, whose radius is near the second zero of $J_0(k_F r)$. The transition is marked by a sharp inward jump from the $n = 2$ orbital. We then increase the rotation rate in a stepwise manner, recording a 150 s trajectory at each rotation rate after waiting at least four minutes following each
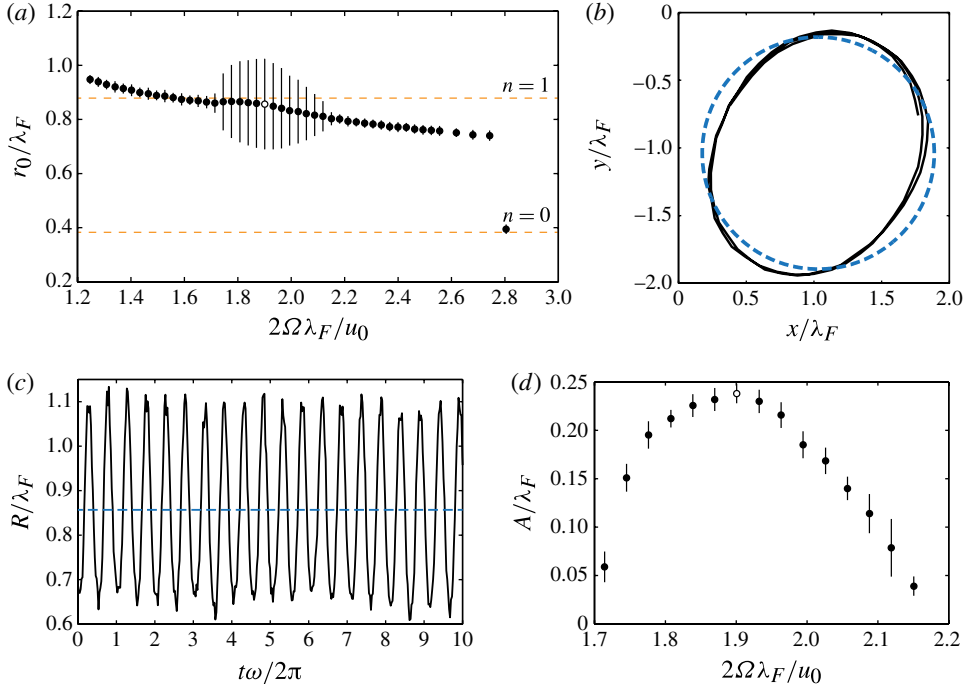
FIGURE 6. (Colour online) (*a*) Evolution of the observed mean radius of curvature r_0 of the $n = 1$ orbital as a function of rotation rate ($\gamma/\gamma_F = 0.961 \pm 0.002$, $u_0 = 12.0$ mm s^{-1}). The error bars extending from each point represent the average deviation from the mean observed radius over the course of a 150 s experiment at fixed Ω. The horizontal dashed lines represent the first two zeros of $J_0(k_F r)$ corresponding to the innermost orbital levels ($n = 0, 1$). The empty marker ($\bigcirc$) denotes the location of the largest observed fluctuations in the radius of curvature. (*b*) A 5 s sample of the trajectory (solid curve) at the point of largest amplitude fluctuations, shown with a circle of equivalent mean radius (dashed). (*c*) Time trace of the instantaneous radius of curvature as it oscillates about a mean radius $R/\lambda_F = 0.86$. (*d*) Amplitude of wobbling motion (A/λ_F) as a function of the rotation rate (Ω) for the wobbling states apparent in panel (*a*).

change. This process is repeated until the walker exits the $n = 1$ orbital by dropping down to the innermost $n = 0$ orbital.

4.1. *Simple wobbling orbits*

In figure 6, we characterize the $n = 1$ orbital level at a forcing amplitude $\gamma/\gamma_F = 0.961$. In figure 6(*a*), the dependence of the mean radius of curvature on the rotation rate is shown, with error bars reflecting the observed variation. For $2\Omega\lambda_F/u_0 < 1.7$, we observe stable circular orbits. However, as the rotation rate is increased through the range $1.7 < 2\Omega\lambda_F/u_0 < 2.2$, considerable growth and then decay in the variation of the radius of curvature is apparent. As evidenced by the trajectory in figure 6(*b*), this region of heightened variation is marked by nearly elliptical orbits. Plotting a sample time trace of the radius of curvature in figure 6(*c*) indicates a distinctive periodic oscillation. Note that this oscillation has approximately twice the frequency of the orbit ($\tilde{\omega} \approx 2\omega$), as is consistent with the nearly elliptical form of the trajectory. We will refer to these periodic orbits that wobble about a stationary orbital centre
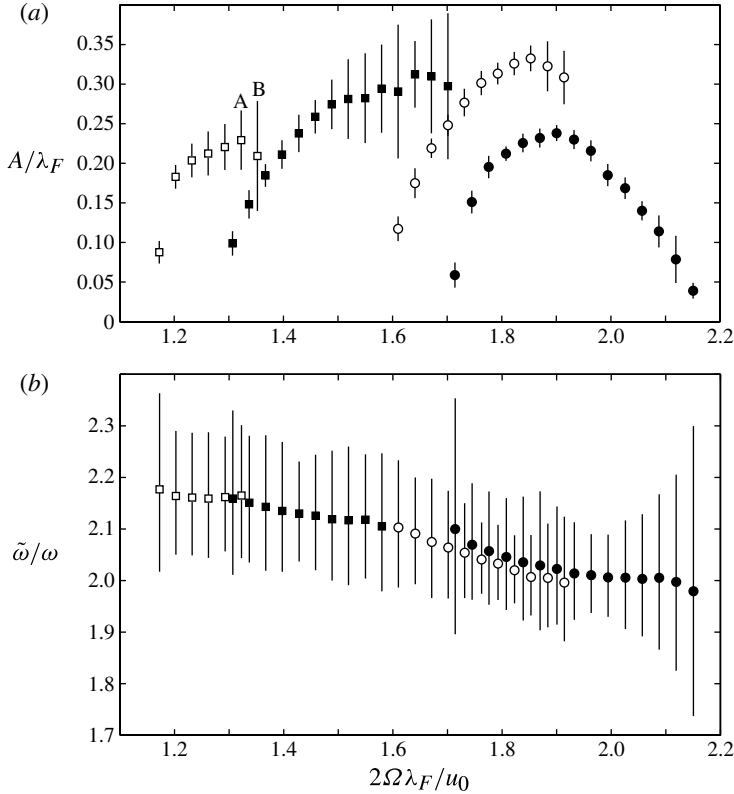
FIGURE 7. The dependence of (*a*) the wobbling amplitude *A* and (*b*) the wobbling frequency $\tilde{\omega}$ on the rotation rate of the bath Ω, for four different values of memory: $\gamma/\gamma_F = 0.978 \pm 0.003$ with $u_0 = 12.4$ mm s^{-1} ($\square$); $\gamma/\gamma_F = 0.974 \pm 0.002$ with $u_0 = 12.3$ mm s^{-1} ($\blacksquare$); $\gamma/\gamma_F = 0.969 \pm 0.005$ with $u_0 = 12.3$ mm s^{-1} ($\bigcirc$); and $\gamma/\gamma_F = 0.961 \pm 0.002$ with $u_0 = 12.0$ mm s^{-1} ($\bullet$, same as figure 6). Each point corresponds to a single 150 s experiment (3000 position measurements) with fixed parameters. The trajectories at the points labelled A and B in panel (*a*) are considered in figures 8 and 9, respectively.

as 'simple' wobbling orbits. For the time trace of each wobbling orbit identified in figure 6(*a*), we report the amplitude of the wobbling in figure 6(*d*), where error bars indicate the minimal variation in this wobbling amplitude at fixed Ω. At this forcing amplitude, a finite window of simple wobbling orbits exists at the $n = 1$ level, each with frequency of approximately 2ω.

What happens at even higher forcing amplitude? The dependence of wobbling amplitude on rotation rate at four different forcing amplitudes γ/γ_F is presented in figure 7(*a*). First we note that the onset of wobbling shifts to lower rotation rates as the forcing amplitude is increased. Second, at higher memory, the trajectories do not return to circular orbits before jumping down to the innermost $n = 0$ mode as Ω is increased. Third, the error bars on the wobbling amplitudes generally increase with memory, reflecting larger fluctuations in the wobbling amplitude. These variations are typically associated with a drifting of the orbital centre, as will be discussed further in §§ 4.2 and 4.3.

We proceed by examining the wobbling frequency $\tilde{\omega}$ more closely. While the wobbling arose near a frequency of 2ω in all cases, there is a weak dependence

on Ω. In figure 7(b), we plot the wobbling frequency as a function of the rotation rate Ω. Here we find a rather surprising result. The data nearly follow a single curve, independent of memory, with the relative wobbling frequency $\tilde{\omega}/\omega$ decreasing monotonically with Ω, a result to be rationalized by Oza *et al.* (2013c). While a trend within a single data set might be expected, the overall collapse to a single curve is striking, indicating that the wobbling frequency is prescribed by the rotation rate of the bath and relatively insensitive to the forcing amplitude. We note that wobbling orbits, each with wobbling frequency $\tilde{\omega} \approx 2\omega$, were also observed in the $n = 2$, 3 and 4 orbitals.

4.2. *Drifting wobbling orbits*

In figure 7(a), significant variation in the wobbling amplitude is evident for certain fixed experimental parameters, particularly at high memory and high Ω. We now consider orbits with large wobbling amplitude corresponding to points A and B in figure 7(a). To better characterize the walker's motion, we track not only the trajectory's local radius of curvature, but the location of the orbital centre as well. The orbital centre at any point is computed by fitting a circle to a length of trajectory corresponding to one orbital period ($t = 2\pi/\omega$) using a least-squares method. The centre of the fitted circle is defined as the orbital centre for that portion of the trajectory. For example, using this method for a simple wobbling orbit such as that in figure 6(b) indicates negligible drift ($<0.1\lambda_F$) of the orbital centre.

In figure 8(a), we present a sample time trace of the local radius of curvature of the drifting wobbling orbit observed at $2\Omega\lambda_F/u_0 = 1.32$ and $\gamma/\gamma_F = 0.978$. In contrast to the stable wobbling observed at lower memory (figure 6c), clear fluctuations in the amplitude arise. A pronounced wobbling is apparent in the trajectory of the walker (figure 8b): the trajectory strongly deviates from a circle. Moreover, the orbit is no longer wobbling about a fixed point: the orbital centre moves in a nearly circular orbit with radius approximately $0.2\lambda_F$. An extended trajectory of the orbital centre (figure 8c) shows that it continues to move along a nearly circular trajectory, albeit with a slight linear drift. In figure 8(d), the coordinates of the orbital centre are plotted with respect to time, indicating that the motion is nearly periodic with a frequency an order of magnitude less than that of the walker's $n = 1$ orbital frequency.

4.3. *Wobble-and-leap dynamics*

We now consider the effects of increasing the rotation rate to $2\Omega\lambda_F/u_0 = 1.35$ while keeping the forcing amplitude fixed, thus probing deeper into the region of unstable circular orbits. In figure 9(a), a sample time trace of the radius of curvature is presented. We now see alternating periods of increasing and decreasing wobbling amplitude. While this process is not precisely periodic, the distinct pattern of growth and collapse is persistent. The walker's trajectory (figure 9b) suggests that there is also a net motion of the orbital centre, which follows a peculiar pattern. In particular, periods of negligible motion of the orbital centre are punctuated by relatively rapid leaps to a new location. Comparing figures 9(c) and 9(a) indicates that the bursts of relatively rapid motion of the orbital centre coincide with the periods of rapid decay in wobbling amplitude. We thus arrive at the following physical picture of 'wobble-and-leap' dynamics. A walker executes a nearly stationary orbit with a wobbling amplitude that grows progressively until it reaches a critical wobbling amplitude, approximately $A/\lambda_F = 0.35$. This wobbling of increasing amplitude is then interrupted by a relatively rapid leap phase, in which the wobbling amplitude is greatly reduced, and the orbital centre shifts. The process then repeats itself.
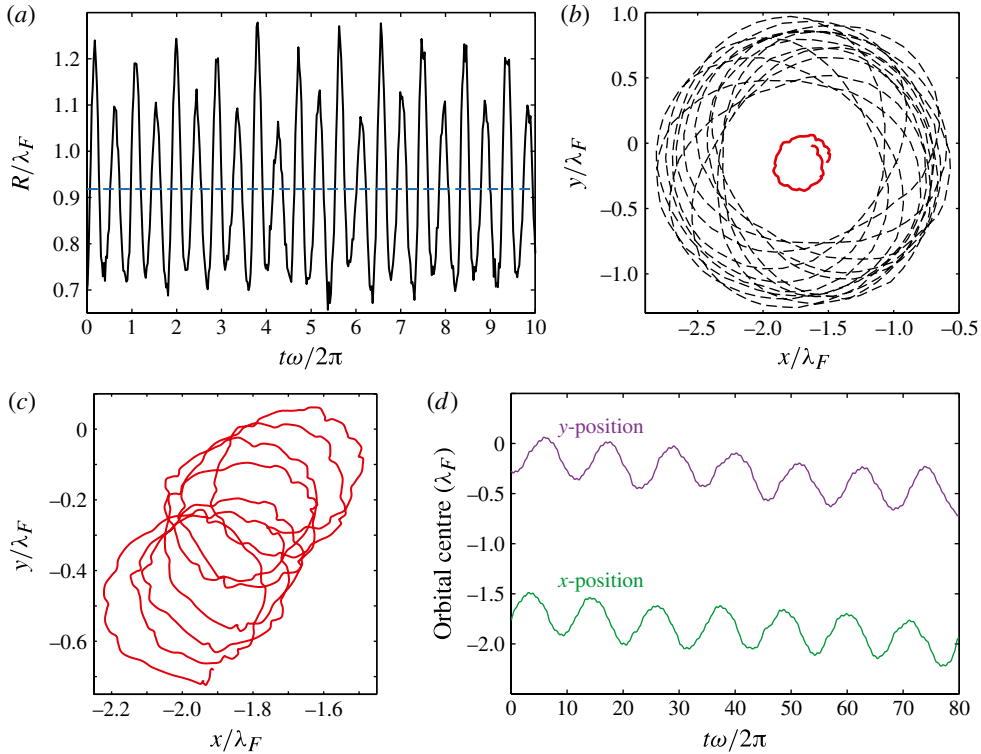
FIGURE 8. (Colour online) Drifting wobbling orbits observed for $\gamma/\gamma_F = 0.978 \pm 0.003$ and $2\Omega\lambda_F/u_0 = 1.32$ with $u_0 = 12.4 \text{ mm s}^{-1}$ (point A in figure 7a). (a) Time trace of the instantaneous radius of curvature that oscillates about a mean radius $R/\lambda_F = 0.92$. (b) Sample droplet trajectory (dashed curve) of 30 s duration, shown with the trajectory of the orbital centre (solid curve). (c) Extended trajectory of the orbital centre: a trace of 180 s is shown. (d) Time evolution of the (x, y) position of the orbital centre, corresponding to the trajectory in panel (c). Data in panels (a–d) are from the same experiment.

An extended trajectory of the orbital centre is presented in figure 9(d), which demonstrates that this wobble-and-leap process is robust and repeated continuously. The approximate locations of the transiently stable orbital centres are highlighted. Figure 9(e) indicates the time evolution of the orbital centre. The plateau regions indicate that the orbital centre is relatively stationary, corresponding to the wobbling phase; thereafter, brief periods of relatively large slope arise corresponding to the 'leaps'. While the time of a single wobble-and-leap cycle varies, the distance between successive centres is nearly constant. For this experiment, the average leap distance was $(0.36 \pm 0.05)\lambda_F$, very close to the first zero of $J_0(k_F r)$, at $0.383\lambda_F$, which corresponds to the radius of the $n = 0$ orbit. No preferred leaping direction was apparent.

The trajectories corresponding to the data sets in figure 7(a) at the highest forcing amplitudes ($\gamma/\gamma_F = 0.978$ and 0.974) have a similar evolution as the rotation rate is increased beyond the onset of wobbling. Near the onset, the wobbling is of relatively small and constant amplitude, and the orbital centre is effectively stationary for the duration of the experiment; here, we have simple wobbling orbits. As the rotation rate is increased further, the wobbling amplitude begins to fluctuate and the orbital centre
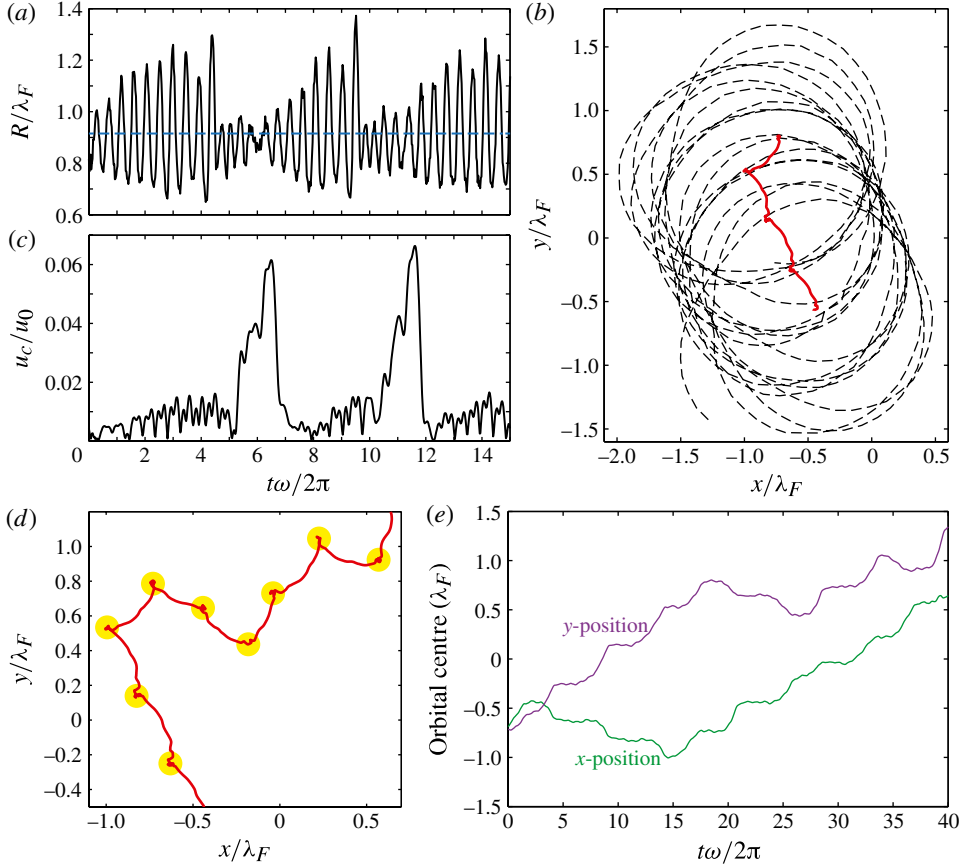
FIGURE 9. (Colour online) Wobble-and-leap dynamics. Results for $\gamma/\gamma_F = 0.978 \pm 0.003$ and $2\Omega\lambda_F/u_0 = 1.35$ with $u_0 = 12.4$ mm s^{-1} (point B in figure 7a). (a) Time trace of the instantaneous radius of curvature that oscillates about a mean radius $R/\lambda_F = 0.92$. (b) Sample droplet trajectory (dashed curve) of 37.5 s duration, shown with the trajectory of the orbital centre (solid curve). (c) Drift speed of the orbital centre (u_c) corresponding to the data in panel (a). (d) Extended trajectory of orbital centre: a trace of 85 s is shown. Transiently stable orbital centres are highlighted via shading. (e) Time evolution of the (x, y) position of the orbital centre, corresponding to the trajectory in panel (d). Data in panels (a–e) are from the same experiment.

begins to drift slowly, often in small circular motions. Beyond this point, we observe the wobble-and-leap dynamics, characterized by periods of wobbling of increasing amplitude with a transiently stable orbital centre, punctuated by a rapid shift to a new location where the growth of the wobbling is reinitiated. Increasing the forcing amplitude even further leads to ever more complex trajectories.

5. Complex trajectories and multimodal statistics

Figure 10(a,b) show two sample trajectories obtained with identical experimental parameters, except for the forcing amplitude γ/γ_F. We see that the stable circular orbit (figure 10a) destabilizes into a complex trajectory (figure 10b) in response to the increased memory. In figure 10(c), we show a sample time trace of the local radius
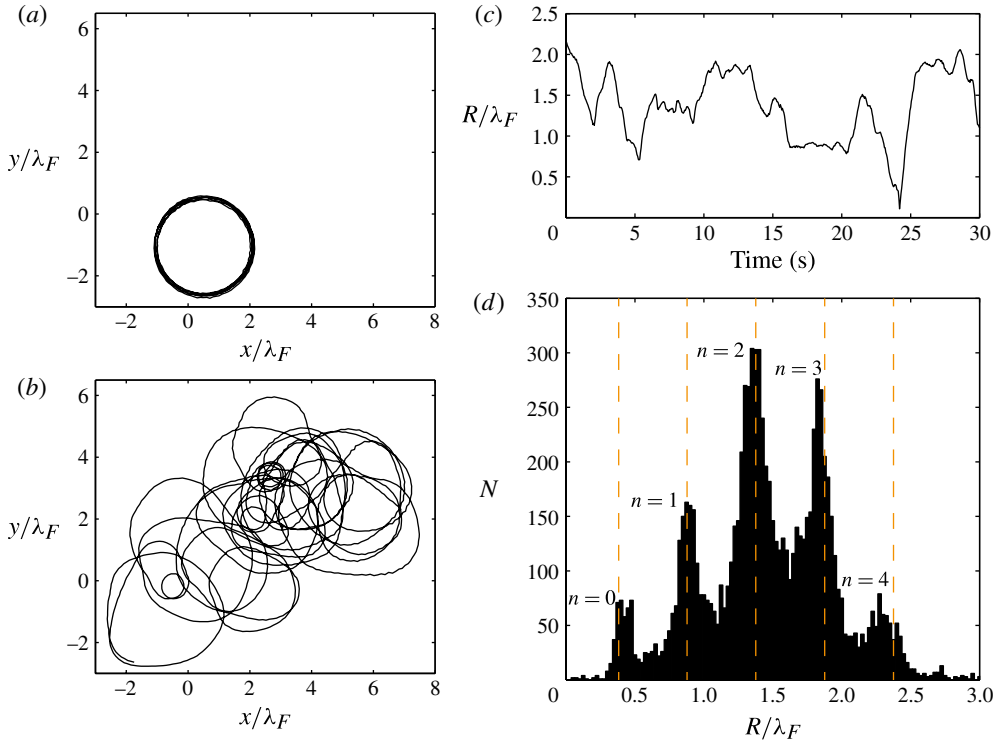
FIGURE 10. (Colour online) (*a*) Observed circular trajectory with $\gamma/\gamma_F = 0.922 \pm 0.004$, $u_0 = 9.5 \text{ mm s}^{-1}$ and $\Omega = 0.98 \text{ rad s}^{-1}$, in the rotating frame. (*b*) Complex observed trajectory at the same rotation rate Ω but increased forcing, $\gamma/\gamma_F = 0.988 \pm 0.002$, $u_0 = 11.3 \text{ mm s}^{-1}$, in the rotating frame. (*c*) Sample time trace of the local radius of curvature. (*d*) Histogram of the local radius of curvature; 9130 measurements were taken over ≈ 8 min. Dashed vertical lines represent the zeros of the Bessel function $J_0(k_F r)$ corresponding to the radii of the unstable circular orbits. The bin size in panel (*d*) is $0.025\lambda_F$. Data presented in panels (*b–d*) are from the same experiment.

of curvature R of the trajectory presented in figure 10(*b*), which indicates that there are specific preferred radii of curvature. The histogram of R (figure 10*d*) indicates that, even when its trajectory is complex and unpredictable, the walker still responds to the quantizing wave force imposed by its pilot-wave field. Specifically, the peaks of the histogram correspond closely to the zeros of the Bessel function $J_0(k_F r)$, indicated by vertical dashed lines corresponding to the quantized orbital radii in the system (figure 4). Thus, while at any given moment it is practically impossible to predict the walker's trajectory, a coherent statistical pattern emerges: the droplet tends to move along curves with radius of curvature R corresponding to the unstable circular orbits, which occur roughly at integer multiples of $\lambda_F/2$. Despite the orbital solutions being unstable, they leave their mark on the walker's statistics.

In this high-memory limit, the walker is freed from its stable orbits to switch erratically between several orbital levels. But how does this transition come about and what determines which states are accessible? In figure 11(*a–c*) we present three different probability distributions for identical system parameters but increasing memory. In figure 11(*a*), the single peak reflects the quantized circular orbit at
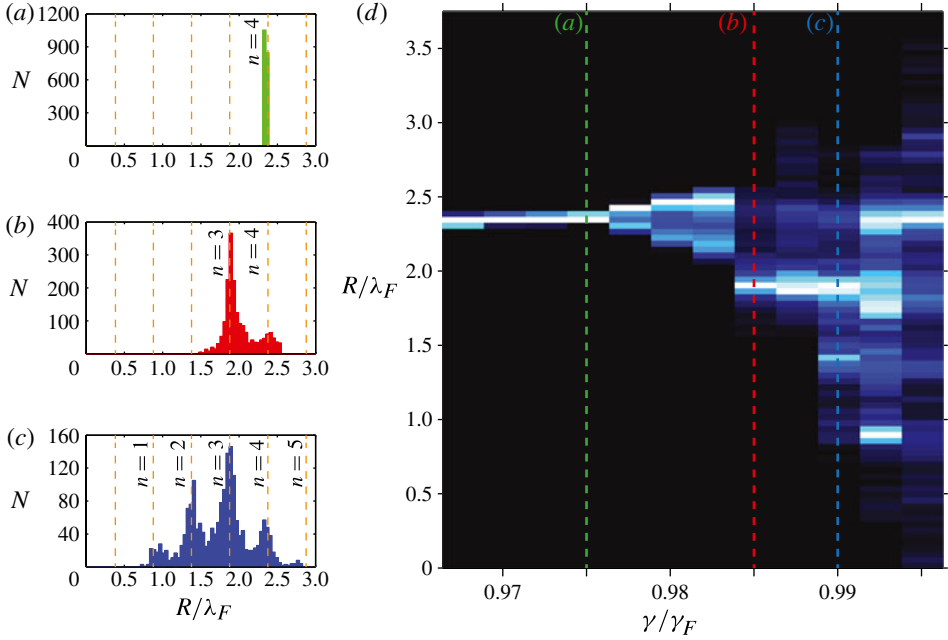
FIGURE 11. (Colour online) The dependence of the orbital statistics on the path memory. (*a*–*c*) Three sample probability distributions at the same rotation rate ($\Omega = 0.79$ rad s^{-1}) for increasing forcing amplitudes: (*a*) $\gamma/\gamma_F = 0.975 \pm 0.002$, (*b*) $\gamma/\gamma_F = 0.985 \pm 0.002$ and (*c*) $\gamma/\gamma_F = 0.990 \pm 0.002$. (*d*) Probability distribution of the radius of curvature R as a function of the forcing amplitude γ/γ_F at a fixed rotation rate ($\Omega = 0.79$ rad s^{-1}). The brightest segment in each vertical column corresponds to the radius with the highest probability at that memory. The vertical dashed lines correspond to the three probability distributions shown in panels (*a*–*c*). The free walking speed is $u_0 = 11.8$ mm s^{-1} at $\gamma/\gamma_F = 0.968 \pm 0.002$. Each column represents 1900 measurements of the local radius of curvature taken over an experiment lasting 100 s. The bin size is fixed at $0.04\lambda_F$.

the $n = 4$ level arising at $\gamma/\gamma_F = 0.975$. As the memory is increased to $\gamma/\gamma_F = 0.985$ (figure 11*b*), the walker can access two orbital levels, namely $n = 3$ and $n = 4$. When the memory is increased to $\gamma/\gamma_F = 0.990$ (figure 11*c*), even more states become accessible, with each peak in the probability distribution corresponding to an unstable quantized orbit.

This progression is characterized comprehensively in figure 11(*d*), which includes the three probability distributions presented in figure 11(*a*–*c*) at the positions denoted by the dashed vertical lines. Each vertical column represents a probability distribution for the radius of curvature of a single experiment at fixed parameters. Up to approximately $\gamma/\gamma_F = 0.975$, a stable circular orbit persists in the $n = 4$ orbital. Beyond this point, the single peak at $n = 4$ begins to spread, reflecting the onset of wobbling of increasing amplitude. At a critical point, when the wobbling amplitude becomes sufficiently large ($\gamma/\gamma_F = 0.985$), the walker escapes its confinement to the $n = 4$ orbital and drifts between multiple unstable orbital levels, as is permissible by virtue of the orbital degeneracy. As the memory is further increased, an increasing number of orbital states are accessible, each leaving their signature on the probability distribution in the form of a distinct peak. While the trajectory is disordered and complex, in each case the statistical behaviour of the walker can be described in terms
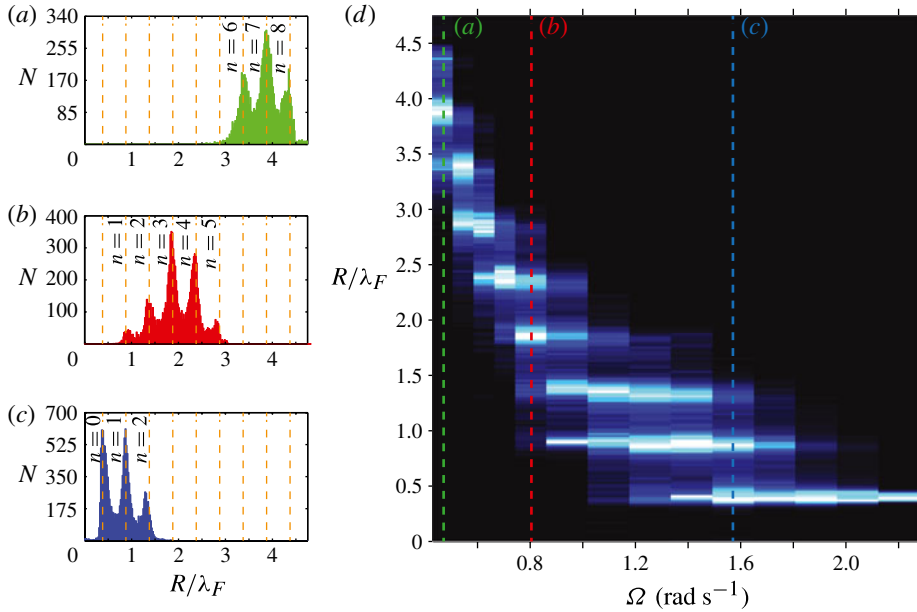
FIGURE 12. (Colour online) The dependence of the orbital statistics on the rotation rate Ω. (*a–c*) Three sample probability distributions at the same forcing amplitude ($\gamma/\gamma_F = 0.988 \pm 0.003$) for increasing rotation rate: (*a*) $\Omega = 0.47$ rad s^{-1}, (*b*) $\Omega = 0.79$ rad s^{-1} and (*c*) $\Omega = 1.57$ rad s^{-1}. (*d*) Probability distribution of the radius of curvature R as a function of the rotation rate Ω at fixed forcing amplitude ($\gamma/\gamma_F = 0.988 \pm 0.003$) and free walking speed ($u_0 = 12.4 \pm 0.2$ mm s^{-1}). The brightest segment in each vertical column corresponds to the radius with the highest probability at that rotation rate. The vertical dashed lines correspond to the three probability distributions shown in panels (*a–c*). Each column represents a minimum of 4900 measurements of the local radius of curvature taken over an experiment lasting at least 250 s. The bin size is fixed at $0.02\lambda_F$.

of a multimodal probability distribution with each peak centred at the radius of an unstable orbital level.

The influence of the rotation rate Ω on the form of the probability distribution for the radius of curvature R at fixed memory ($\gamma/\gamma_F = 0.988$) is illustrated in figure 12. Three sample probability distributions are provided in figure 12(*a–c*) for three different rotation rates. In each case, the walker accesses several orbital levels, with the mean R decreasing as the rotation rate is increased. Figure 12(*d*) provides a complete characterization of the dependence of the probability distribution on rotation rate Ω. As in figure 11(*a*), each vertical column corresponds to a probability distribution obtained for fixed experimental parameters. In general we see a shift from larger to smaller orbits as the rotation rate is increased, consistent with the trend evident in figure 4. Here, however, the walker may in general switch between several accessible orbitals during a single experiment. At the highest rotation rate considered, we see that the innermost circular orbit, $n = 0$, becomes stable.

The results presented in figures 11 and 12 indicate the manner in which the form of the probability distribution depends on the two control parameters, γ/γ_F and Ω. In general, γ/γ_F controls the number of accessible states, while Ω determines their mean radius. The distribution takes a multimodal form owing to the underlying pilot-wave dynamics, specifically to the dynamic imprint of the unstable orbits.

We note that, for the very high memories considered here, the wave field is seen to extend to the edges of the fluid tray (figure 3*c*,*d*), which suggests the possible significance of boundary effects. Moreover, Harris *et al.* (2013) have demonstrated that spatial confinement of a walker to a circular corral can also result in complex trajectories at high memory. However, in the current study, despite the similar forcing amplitudes considered, the region of confinement is significantly larger. In the absence of rotation, walkers in the current study follow simple periodic circular trajectories, moving along the boundary at a constant speed. In order for irregular trajectories to arise at high memory, the bulk system rotation must be applied. Finally, we note that, at high memory, irregular trajectories with multimodal statistics are also observed in our numerical simulations of this rotating system, wherein boundaries are entirely absent (Oza *et al.* 2013*c*). Direct comparison with these numerical results suggests that boundary effects are not significant in our experiments.

6. Conclusions

We have characterized the influence of path memory on the dynamics of droplets walking in a rotating frame. At short path memory, the droplet executes a stable circular orbit whose radius decreases continuously and monotonically with increasing rotation rate. As the memory is increased, the orbiting droplet interacts with its own wake, resulting in the quantization of both radius and frequency (Fort *et al.* 2010). We have demonstrated that the orbital quantization does not represent the high-memory limiting behaviour of the system, but arises only within a finite range of memory. Moreover, the quantized orbits do not all appear at a single value of memory; rather, the number of quantized states increases with increasing memory, with each level being stable only within a finite range of memory. The smallest orbits have the shortest orbital period, and so are the first to be quantized by the wave field.

As the memory is increased progressively, the stable quantized circular orbits are superseded in turn by wobbling orbits with stationary, drifting, then leaping orbital centres, and ultimately by irregular trajectories. We have detailed this progression for the $n = 1$ orbital level. As the memory is increased, the circular orbit gives way to a simple wobbling state, characterized by a periodic fluctuation in the local radius of curvature and a stationary orbital centre. Thereafter, a smooth drift of the orbital centre arises, accompanied by a fluctuating wobbling amplitude. Subsequently, wobble-and-leap dynamics arise in which orbital motion with a fixed orbital centre and a growing wobbling amplitude is punctuated by brief periods of rapid motion of the orbital centre. Finally, the wobbling is of sufficient amplitude to free the walker from its orbital confinement. An increasing number of orbital levels thus become accessible, and irregular trajectories emerge. In the high-memory limit, the radius of curvature at any instant is difficult to predict, as the walker switches erratically between arcs with curvatures corresponding to the unstable quantized levels. This particular feature of pilot-wave hydrodynamics leaves a distinct signature on the probability distribution of the radius of curvature; specifically, it is multimodal with peaks at the radii of the underlying unstable orbital states. The statistical pattern is thus a direct consequence of the underlying pilot-wave dynamics and the persistent influence of the unstable orbital states on the trajectory. The entire progression reported here will be rationalized through accompanying theoretical developments (Oza *et al.* 2013*a*,*c*).

It is interesting to consider our results in light of recent investigation of droplets walking in a central force field (Perrard *et al.* 2013). By encapsulating a ferrofluidic droplet in silicone oil and applying a non-uniform external magnetic field,

Perrard *et al.* were able to characterize the motion of a walker in a harmonic potential. At high memory, they observe circular orbits as well as more complex periodic trajectories (e.g. lemniscates) whose form is consistent with quantization in both energy (as prescribed by the orbital radius) and angular momentum. As in our study, switching between periodic states is prevalent at high memory. In their system, there is a fixed orbital centre corresponding to the centre of force. The absence of this constraint in our system allows for the observed drifting and leaping of the orbital centre. While it is more difficult to define the energy of the orbital states in the rotating system, one can interpret the observed quantization in radius of curvature R as reflecting a quantization in angular momentum, mu_0R, about the orbital centre.

Finally, it is important to note that the entire progression from stable quantized orbits to wobbling orbits then irregular trajectories occurs within a few per cent of the Faraday threshold, indicating that uniform, well-controlled vibration is essential for a reliable characterization of the statistical behaviour of the walking droplets.

Acknowledgements

Appendix. Calculation of radius of curvature

We seek to compute the local radius of curvature of the trajectory in the rotating frame. We use an adaptive osculating circle technique. We denote the ith point along the trajectory as p_i. At each point p_i, we first connect that point with a straight line to its nearest neighbours p_{i-1} and p_{i+1}. We then compute the interior angle between segments, $\angle p_{i-1}p_ip_{i+1} = \theta_{i,1}$. Note that, in the continuous limit, each of the segments approaches the local tangent line, so that $\theta_{i,1}$ approaches π. Next, we proceed to calculate the interior angle between segments $p_{i-2}p_i$ and p_ip_{i+2}, which we define as $\theta_{i,2}$. We repeat this procedure by incrementally increasing the value of the second index until we find a $k = k_c$ such that $\pi - \theta_{i,k} > \alpha$, where α is some critical angle that we specify. We then fit a circle to the points $\{p_{i-k_c}, p_i, p_{i+k_c}\}$, and define the radius of this circle, $r_{i,k}$, to be an approximation of the local radius of curvature at point p_i. Additionally, we set a minimum value $k_c \geqslant 2$, which provides good resistance to noise for our data.

In some sense this method is 'adaptive' in that, in general, k_c will be larger for regions of small curvature and smaller for regions of high curvature. We find that this adaptive osculating circle method provides a reasonable noise-resistant algorithm for calculating the radii of curvature in our experiments.

REFERENCES

BENJAMIN, T. B. & URSELL, F. 1954 The stability of the plane free surface of a liquid in vertical periodic motion. *Proc. R. Soc.* A **225**, 505–515.

DE BROGLIE, L. 1926 *Ondes et Mouvements*. Gauthier-Villars.

DE BROGLIE, L. 1987 Interpretation of quantum mechanics by the double solution theory. *Ann. Fond. Louis de Broglie* **12**, 1–23.

DE BRUYN, J. R., LEWIS, B. C., SHATTUCK, M. D. & SWINNEY, H. L. 2001 Spiral patterns in oscillated granular layers. *Phys. Rev.* E **63**, 041305.

BUSH, J. W. M. 2010 Quantum mechanics writ large. *Proc. Natl Acad. Sci.* **107**, 17455–17456.

COUDER, Y. & FORT, E. 2006 Single particle diffraction and interference at a macroscopic scale. *Phys. Rev. Lett.* **97**, 154101.

COUDER, Y., FORT, E., GAUTIER, C. H. & BOUDAOUD, A. 2005 From bouncing to floating: non-coalescence of drops on a fluid bath. *Phys. Rev. Lett.* **94**, 177801.

CROMMIE, M. F., LUTZ, C. P. & EIGLER, D. M. 1993 Confinement of electrons to quantum corrals on a metal surface. *Science* **262**, 218–220.

EDDI, A., FORT, E., MOISY, F. & COUDER, Y. 2009 Unpredictable tunneling of a classical wave–particle association. *Phys. Rev. Lett.* **102**, 240401.

EDDI, A., MOUKHTAR, J., PERRARD, S., FORT, E. & COUDER, Y. 2012 Level splitting at macroscopic scale. *Phys. Rev. Lett.* **108**, 264503.

EDDI, A., SULTAN, E., MOUKHTAR, J., FORT, E., ROSSI, M. & COUDER, Y. 2011 Information stored in Faraday waves: the origin of path memory. *J. Fluid Mech.* **674**, 433–463.

EDDI, A., TERWAGNE, D., FORT, E. & COUDER, Y. 2008 Wave propelled ratchets and drifting rafts. *Europhys. Lett.* **82**, 44001.

FARADAY, M. 1831 On the forms and states of fluids on vibrating elastic surfaces. *Phil. Trans. R. Soc. Lond.* **121**, 319–340.

FORT, E., EDDI, A., BOUDAOUD, A., MOUKHTAR, J. & COUDER, Y. 2010 Path-memory induced quantization of classical orbits. *Proc. Natl Acad. Sci.* **107** (41), 17515–17520.

GOLDMAN, D. I. 2002 Pattern formation and fluidization of vibrated granular layers, and grain dynamics and jamming in a water fluidized bed. PhD thesis, University of Texas at Austin, Austin, TX.

HARRIS, D. M., MOUKHTAR, J., FORT, E., COUDER, Y. & BUSH, J. W. M. 2013 Wavelike statistics from pilot-wave dynamics in a circular corral. *Phys. Rev.* E **88**, 011001.

KUMAR, K. 1996 Linear theory of Faraday instability in viscous fluids. *Proc. R. Soc.* A **452**, 1113–1126.

MOLÁČEK, J. & BUSH, J. W. M. 2013a Drops bouncing on a vibrating bath. *J. Fluid Mech.* **727**, 582–611.

MOLÁČEK, J. & BUSH, J. W. M. 2013b Drops walking on a vibrating bath: towards a hydrodynamic pilot-wave theory. *J. Fluid Mech.* **727**, 612–647.

OZA, A., HARRIS, D. M., ROSALES, R. R. & BUSH, J. W. M. 2013a Pilot-wave dynamics in a rotating frame: on the emergence of orbital quantization. (under review).

OZA, A., ROSALES, R. R. & BUSH, J. W. M. 2013b A trajectory equation for walking droplets. *J. Fluid Mech.* **737**, 552–570.

OZA, A., WIND-WILLASSEN, Ø., HARRIS, D. M., ROSALES, R. R. & BUSH, J. W. M. 2013c Exotic orbits in hydrodynamic pilot-wave theory (in preparation).

PERRARD, S., LABOUSSE, M., MISKIN, M., FORT, E. & COUDER, Y. 2013 Memory driven wave–particle self-organization (under review).

PROTIÈRE, S., BOUDAOUD, A. & COUDER, Y. 2006 Particle wave association on a fluid interface. *J. Fluid Mech.* **554**, 85–108.

REIS, P. M., INGALE, R. A. & SHATTUCK, M. D. 2007 Forcing independent velocity distributions in an experimental granular fluid. *Phys. Rev.* E **75**, 051311.

WALKER, J. 1978 Drops of liquid can be made to float on the liquid. What enables them to do so? *Sci. Am.* **238–6**, 151–158.

WIND-WILLASSEN, Ø., MOLÁČEK, J., HARRIS, D. M. & BUSH, J. W. M. 2013 Exotic states of bouncing and walking droplets. *Phys. Fluids* **25**, 082002.